

Electronic structure of spin frustrated magnets: Mn_3O_4 spinel and postspinel

S. Hirai,^{1,2} Y. Goto,³ A. Wakatsuki,³ Y. Kamihara,³ M. Matoba,³ and W. L. Mao^{1,2}

¹*Department of Geological and Environmental Sciences, Stanford University, California 94305, USA*

²*Stanford Institute for Materials and Energy Sciences,*

SLAC National Accelerator Laboratory, 2575 Sand Hill Road, Menlo Park, CA 94025, USA

³*Department of Applied Physics and Physico-Informatics,*

Keio University, 3-14-1 Hiyoshi, Yokohama 223-8522, Japan

Mn_3O_4 is a spin frustrated magnet that adopts a tetragonally distorted spinel structure at ambient conditions and a CaMn_2O_4 -type postspinel structure at high pressure. We conducted both optical measurements and *ab initio* calculations, and systematically studied the electronic band structures of both the spinel and postspinel Mn_3O_4 phases. For both phases, theoretical electronic structures are consistent with the optical absorption spectra, and display characteristic band-splitting of the conduction band. The band gap obtained from the absorption spectra is 1.91(6) eV for the spinel phase, and 0.94(2) eV for the postspinel phase. Both phases are charge-transfer type insulators. The Mn $3d\ t_{2g}$ and O $2p$ form antibonding orbitals situated at the conduction band with higher energy.

PACS numbers: 71., 75.47.Lx, 75.25.-j

I. INTRODUCTION

Manganese oxides have been exploited for a wide range of technological applications including electrode materials for batteries (MnO_2)¹, ultracapacitors for energy storage devices (Mn_2O_3)², and as electrochromic materials (Mn_3O_4)³. Mn_3O_4 is a unique mixed-valence oxide that adopts a tetragonally distorted spinel structure (Figure 1) at ambient conditions⁴⁻⁹. This phase undergoes a structural phase transition at 15 GPa into a CaMn_2O_4 -type phase, referred to as postspinel (Figure 1), which is quenchable to ambient pressure¹⁰⁻¹². Lattice, spin, and orbital degrees of freedom are strongly coupled in both phases¹²⁻¹⁶. Mn_3O_4 spinel undergoes three magnetic transitions ($T_N = 41$ K, $T_1 = 39$ K, $T_2 = 33$ K)⁸, exhibits pronounced magnetodielectric and magnetoelastic coupling¹³⁻¹⁵, and a quantum phase transition^{6,16}. It adopts three magnetic structures, (i) $T_1 < T < T_N$: a so-called Yafet-Kittel magnetic structure¹⁷ in which Mn^{2+} and Mn^{3+} spins lie on the (1 -1 0) plane in a triangular spin configuration (Yafet-Kittel phase)⁷⁻⁹, (ii) $T_2 < T < T_1$: a conical⁸ or sinusoidal⁹ magnetic structure incommensurate with the chemical unit cell, and (iii) $T < T_2$: a commensurate magnetic structure with the magnetic unit cell of the Yafet-Kittel phase doubled along the [1 1 0] direction. This complicated magnetic structure implies that Mn_3O_4 spinel is a spin frustrated magnet^{13-16,18,19}. Mn_3O_4 postspinel undergoes a giant atomic displacement near its $T_N = 210$ K due to the coupled effect of the metastable structure with the orbital realignment of the Mn^{3+} ion¹². Below 210 K, the postspinel phase of Mn_3O_4 adopts a magnetic structure in which Mn^{3+} spins align antiferromagnetically along the edge-sharing a axis, with a magnetic propagation vector $\mathbf{k}=[1/2,0,0]$ ¹². In contrast, Mn^{2+} spins are geometrically frustrated since they are situated at the center of a honeycomb arrangement of Mn^{3+} spins that are

antiferromagnetically ordered, and exhibit a short-range magnetic order only below 55 K¹².

Therefore, both of these phases are magnetically frustrated^{12-16,18,19}, providing an important playground for systematically studying the electronic band structures of spin frustrated magnets²⁰. Electrical resistivity for the bulk polycrystalline samples are $\approx 10^8\ \Omega\text{cm}$ ²¹ for the spinel phase, and $\approx 10^7\ \Omega\text{cm}$ ¹² for the postspinel phase. Previous studies on the band structure of Mn_3O_4 spinel are limited to theoretical studies using Hartree-Fock²² and density functional theory (DFT) calculations²³, which have significant disagreement in their results. While there are a few studies reported for thin film ($E_g = 2.51$ eV)²⁴ and nanoparticles ($E_g = 2.07$ eV)²⁵ for Mn_3O_4 spinel, no optical studies have been reported for bulk polycrystalline and single crystalline samples of Mn_3O_4 spinel or postspinel.

In this study, we found that both phases of Mn_3O_4 possess characteristic band-splitting of the conduction band. Theoretical electronic structures are consistent with absorption spectra, where the band gap is 1.91(6) eV for the spinel phase and 0.94(2) eV for the postspinel phase. Both phases are charge-transfer type insulators. Mn $3d\ t_{2g}$ and O $2p$ form antibonding orbitals situated at the conduction band with higher energy.

II. EXPERIMENTS

Polycrystalline samples of Mn_3O_4 spinel and postspinel were prepared at ambient and high pressure, respectively¹². The spinel phase was prepared by heating MnCO_3 (Alfa Aesar, 99.99 %) in air at 1400 K for 16 h. The postspinel phase was prepared by pressurizing the spinel phase up to 20 GPa using a cell fitted with polycrystalline diamond double toroidal anvils, followed by slow decompression to ambient pressure. Purity of the samples was examined by using synchrotron X-ray

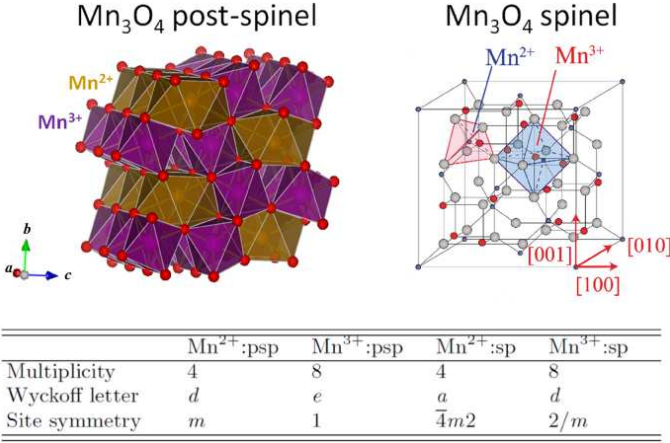


FIG. 1: (color online) Schematic image of the crystal structure of Mn_3O_4 postspinel (psp) (space group: $Pbcm(57)$) and spinel (sp) (space group: $I41/amd(141)$). Multiplicity, Wyckoff letter, and site symmetry of Mn^{2+} and Mn^{3+} are listed as a reference.

diffraction (XRD) ($\lambda = 0.041222$ nm) at beamline 16-BMD of the advanced photon source (APS), Argonne National Laboratory (ANL)¹².

Total diffuse reflectance spectra of Mn_3O_4 spinel and postspinel were measured using a spectrometer equipped with an integrating sphere (Hitachi High-Tech, U-4100). Al_2O_3 powder was used as a standard reference. Then, the diffuse reflectance spectra were converted to absorption spectra using the Kubelka-Munk equation, $(1-R)^2/2R = \alpha/s$, where R , α and s denote reflectivity, absorption coefficient and scattering factor, respectively²⁶. The optical band gap was deduced from the linear extrapolation of absorption spectra with energy.

Ab initio calculations were performed using the plane-wave projector augmented-wave (PAW) method^{27,28} implemented in Vienna *Ab initio* Simulation Package (VASP) code^{29,30}. Three different approximations to treat exchange-correlation potential were applied: (i) the generalized gradient approximation (GGA) by the Perdew-Becke-Ernzerhof (PBE) method³¹, (ii) the PBE plus a on-site Coulomb repulsion (U) term following the approach of Dudarev³² for effective value of the Coulomb parameter ($U_{eff} = U - J$, where J being an intra-atomic exchange parameter), and (iii) the hybrid functionals by the Heyd, Scuseria, and Ernzerhof (HSE06) method³³, where correlation is described in GGA (PBE) and its exchange is a mixture of 25 % exact Hartree-Fock and 75 % PBE exchange. We used the lattice constants of $a = 0.5756$ nm and $c = 0.9439$ nm at 4.2 K⁷ for the spinel phase and $a = 0.3020$ nm, $b = 0.9842$ nm, and $c = 0.9568$ nm at 60 K¹² for the postspinel phase, which were determined by neutron diffraction. We used the lattice constants at 60 K for the postspinel phase since the atomic coordinates could not be determined from neutron diffraction due to the contribution of short-range ordered Mn^{2+} spins¹². Also a $2 \times 1 \times 1$ supercell was con-

structed to investigate the magnetic structure of postspinel. The Brillouin zone was sampled by a $3 \times 3 \times 2$ and a $3 \times 3 \times 2$ Monkhorst-Pack grid³⁴ for the spinel and postspinel phases, respectively. A cutoff of 450 eV was chosen for the plane-wave basis set for both phases. Hellmann-Feynman forces were reduced until 0.5 eV nm⁻¹ for the spinel phase, while the atomic coordinates for the postspinel phase were fixed at the initial input value due to its metastable nature¹².

III. RESULTS AND DISCUSSION

Figure 2 shows the absorption spectra of Mn_3O_4 spinel and postspinel, converted from diffuse reflectance spectra using the Kubelka-Munk equation²⁶. Red and blue lines are guide for estimating the optical band gap of the two energy levels of the conduction band in these phases. *Ab initio* calculations were also performed in order to obtain the theoretical band gap. Table I shows the experimental band gap from optical absorption spectra and the theoretical band gap from *ab initio* calculations for Mn_3O_4 spinel and postspinel. Both methods show a consistent band structure with characteristic band-splitting of the conduction band (Table I and Figure 3). The band gap obtained from optical absorption spectra is $1.91(6)$ eV for the spinel phase and $0.94(2)$ eV for the postspinel phase. The calculated band structure will be presented for both phases, and then their electronic structures will be further discussed.

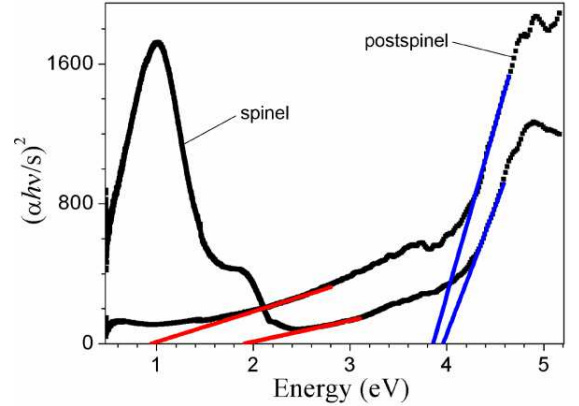


FIG. 2: (color online) Absorption spectra of Mn_3O_4 spinel and postspinel, converted from diffuse reflectance spectra using the Kubelka-Munk equation, $(1-R)^2/2R = \alpha/s$, where R , α and s denote reflectivity, absorption coefficient and scattering factor, respectively²⁶. Red and blue lines are extrapolated to the energy axis, providing an estimate of optical band gap for these phases.

First, the band structure of Mn_3O_4 spinel will be discussed. Figure 3(a) shows the DOS calculated for Mn_3O_4 spinel with $U - J = 4, 5, 6$ eV. HSE06 calculations (Figure 4(a)) was conducted as well as PBE+U calculations, and all these calculations give a widely spread valence

Methods	$E_{g1:sp}$ (eV)	$E_{g2:sp}$ (eV)	$E_{g1:psp}$ (eV)	$E_{g2:psp}$ (eV)
U-J=4 eV	1.36	3.17	0.36	2.81
U-J=5 eV	1.46	3.47	0.55	3.40
U-J=6 eV	1.48	3.60	0.56	3.71
HSE06	2.61	4.17	1.34	3.56
Experimental	1.91(6)	3.96(9)	0.94(2)	3.86(6)

TABLE I: Theoretical (calculated by PBE+U, HSE06) and experimental (deduced from optical absorption spectra) band gap for Mn_3O_4 spinel (sp) and postspinel (psp). The optical band gaps for the two energy levels of the conduction band are denoted as E_{g1} and E_{g2} , respectively.

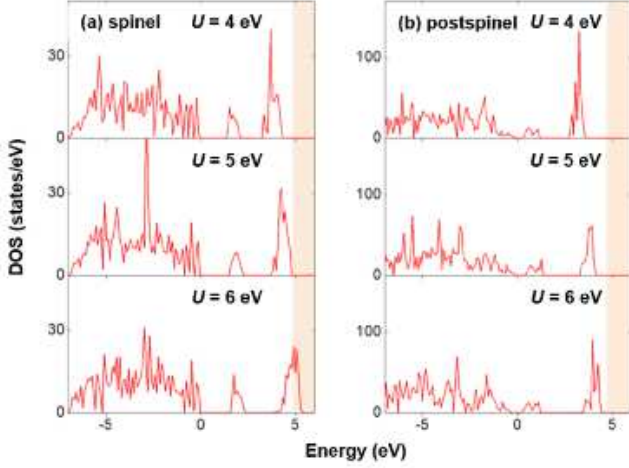


FIG. 3: (color online) Up-spin densities of states in Mn_3O_4 spinel and postspinel calculated with U-J = 4, 5, 6 eV in PBE+U method. The work function of manganese oxides (e.g. MnO) is in a range of 4.6-6.6 eV³⁵, shaded pink as a reference.

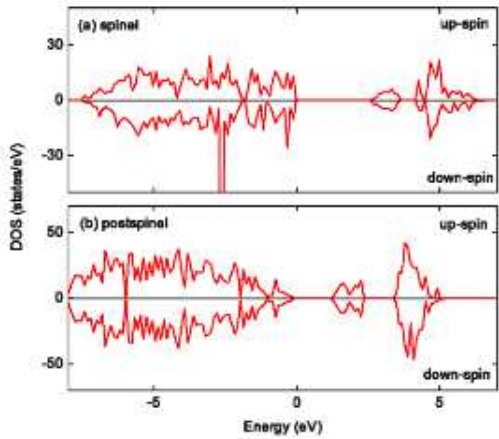


FIG. 4: (color online) Densities of states in Mn_3O_4 spinel and postspinel calculated in HSE06 method.

band and a characteristic band-splitting of the conduction band (Figure 3(a) and Figure 4(a)). This band-splitting of the conduction band is allowed since the work function of manganese oxides (e.g. MnO) is in a range of

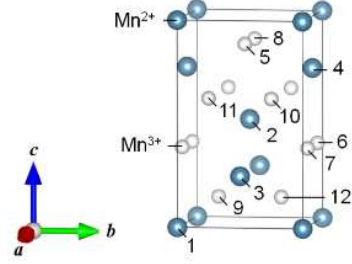


FIG. 5: (color online) Spin configurations of Mn and the total energy differences (ΔE) with respect to the ferromagnetic (FM) solutions for Mn_3O_4 spinel with U-J = 5 eV in PBE+U method. The calculated magnetic moment of Mn^{2+} and Mn^{3+} are 4.6 μ_B /atom and 3.9 μ_B /atom, respectively. The calculated magnetic moment of Mn^{2+} and Mn^{3+} are in good agreement with the previously reported ordered moment of 4.65 μ_B /atom and 3.55 μ_B /atom at 4.2 K obtained from neutron diffraction⁷.

4.6-6.6 eV³⁵. The band gap and the energetically most stable magnetic structure (Figure 5, referred to as FIM 6 in a previous study²²) of Mn_3O_4 spinel obtained from the *ab initio* calculations is consistent with Chartier et al²² and the previously reported cell-doubled magnetic structure below 33 K obtained from neutron diffraction studies⁷⁻⁹.

Next, the band structure of Mn_3O_4 postspinel will be discussed. The band gap of the postspinel phase (0.94(2) eV from optical absorption spectra) is about 1 eV smaller than that of the spinel phase (Table I). Figure 3(b) and Figure 4(b) show the DOS calculated for Mn_3O_4 postspinel, where all the calculations give a wide valence band and characteristic band-splitting of the conduction band, similar to what was observed for the spinel phase. The two most stable magnetic structure calculated by this study (AFM 3 and AFM 7 in Figure 6) does not contradict with the short-range magnetic order of Mn^{2+} spins below 55 K since the canted Mn^{2+} spins allow ferromag-

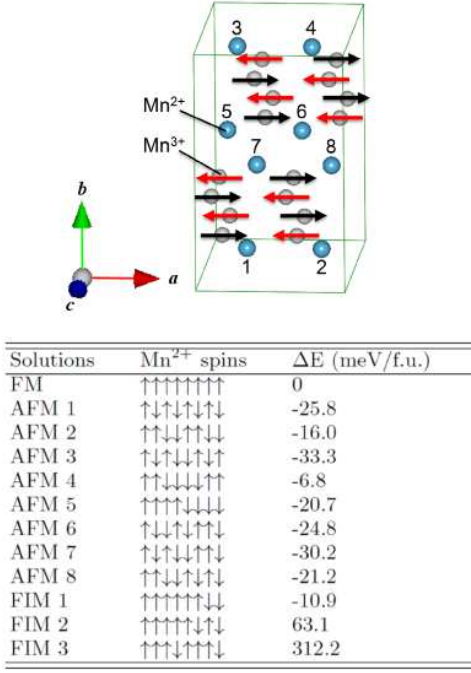


FIG. 6: (color online) Spin configurations of Mn²⁺ and the total energy differences (ΔE) with respect to the ferromagnetic (FM) solutions for Mn₃O₄ postspinel with U-J = 5 eV in PBE+U method. Black and red arrows denote the spin configuration of Mn³⁺, which was fixed to an antiferromagnetic (AFM) order along the crystallographic a axis, with a magnetic propagation vector $\mathbf{k} = [1/2, 0, 0]$ ¹². The calculated magnetic moment of Mn²⁺ and Mn³⁺ are 4.7 μ_B /atom and 4.0 μ_B /atom, respectively. The calculated magnetic moment of Mn³⁺ is in good agreement with the previously reported ordered moment of 3.49(2) μ_B /atom at 60 K obtained from neutron diffraction¹². The calculated magnetic moment of Mn²⁺ does not contradict with the short-range magnetic order of Mn²⁺ spins below 55 K¹² since the spin canting was not considered in PBE method.

netic net magnetization¹². The energy difference between AFM 3 and AFM 7 (Figure 6) is only 3.1 meV/f.u., which is comparable with the thermal fluctuation of ≈ 4.7 meV at 55 K. Therefore, *ab initio* calculation demonstrates that Mn₃O₄ postspinel is a spin frustrated magnet and the small energy difference between two AFM solutions is in harmony with the experimentally observed short-range magnetic order below 55 K¹². Since the calculated band gap is in good agreement with the optical absorption spectra and the most stable magnetic structure does not contradict with the neutron diffraction studies for both phases^{7-9,12}, the electronic band structure of Mn₃O₄ is further explored on the basis of *ab initio* calculation. Hereafter we will employ the up-spin DOS with U-J = 5 eV for the phases, since the selection of U-J parameter does not change its DOS structure to a great extent. Figure 7 demonstrates that Mn 3d orbitals are widely spread over the valence band, and they have significant overlap with the O 2p orbitals. Although the band width becomes narrower, this feature is maintained

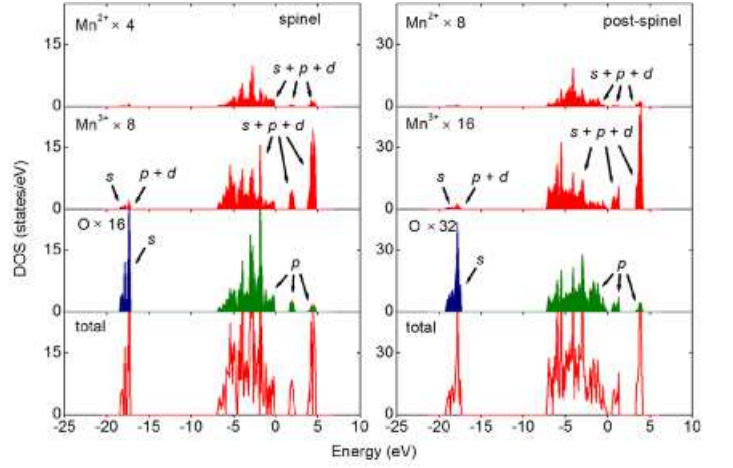


FIG. 7: (color online) Up-spin DOS calculated with U-J = 5 eV for each atom (Mn²⁺, Mn³⁺ and O) and total DOS in Mn₃O₄ spinel and postspinel. More than 80 % of the $s+p+d$ orbitals of Mn are 3d orbitals.

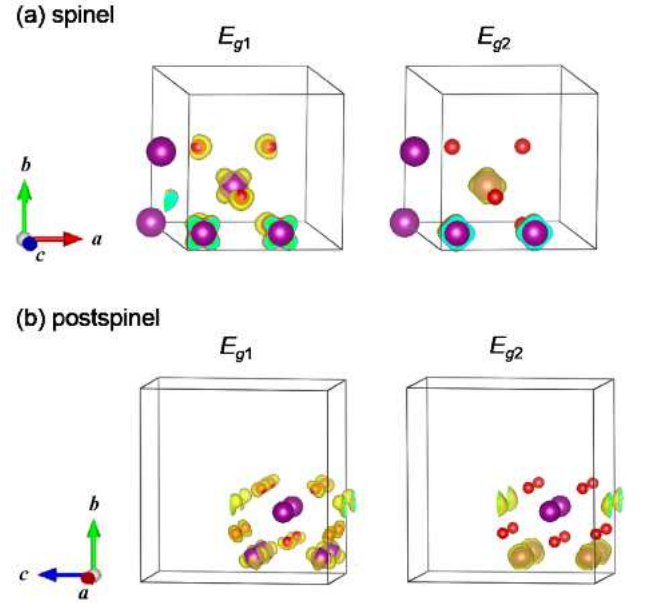


FIG. 8: (color online) Theoretical local charge density of Mn³⁺O₆ octahedra in Mn₃O₄ spinel and postspinel integrated over the two energy levels of the conduction band, denoted as E_{g1} and E_{g2} . Yellow shading represents the charge distribution in Mn and O.

for the conduction band as well.

Mn₃O₄ spinel has a tetragonal symmetry (space group: $I41/amd(141)$), which results in the Mn 3d orbitals being split into three nondegenerate levels and a doubly degenerate level. Figure 8(a) shows the theoretical local charge density map of Mn³⁺O₆ octahedra calculated for the two energy levels of the conduction band in Mn₃O₄ spinel. Since the theoretical DOS of Mn²⁺ electrons in the conduction band is very small, the theoretical DOS

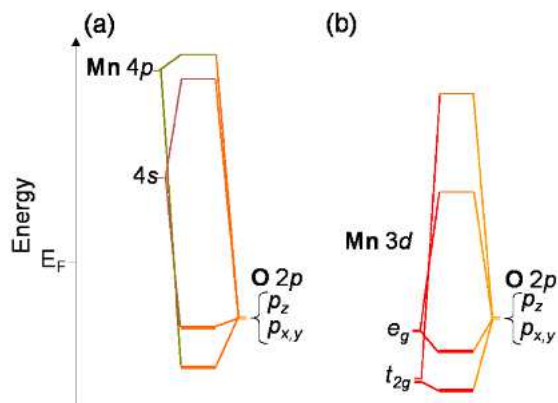


FIG. 9: (color online) Schematic view of the energy diagram of Mn and O for both phases in Mn_3O_4 , provided that Mn $3d$ orbitals pointing toward the O atom are t_{2g} and the rest are e_g . (a) An extracted diagram for Mn $4s$, Mn $4p$, and O $2p$. (b) An extracted diagram for Mn $3d$ and O $2p$.

of Mn^{3+} electrons sufficiently represent the total DOS for Mn $3d$ electrons in the conduction band. The multiplicity, Wyckoff letter, and site symmetry for Mn^{3+} in Mn_3O_4 spinel are 8, d , and $2/m$, respectively. Provided that the Mn $3d$ orbitals pointing toward the O atom are t_{2g} and the rest are e_g , the projection of charge distribution for Mn $3a$ electrons (Figure 8(a)) suggests that the conduction band with lower energy (E_{g1}) corresponds to Mn $3d$ t_{2g} , and the conduction band with higher energy (E_{g2}) corresponds to Mn $3d$ e_g (Figure 9).

Mn_3O_4 postspinel has an orthorhombic symmetry (space group: $Pbcm(57)$), which results in the Mn $3d$ levels being five nondegenerate levels. The multiplicity, Wyckoff letter, and site symmetry of Mn^{3+} in Mn_3O_4 postspinel are 8, e , and 1, respectively. Analogous to the spinel phase, the projection of charge distribution for Mn $3d$ electrons of Mn_3O_4 postspinel (Figure 8(b)) suggests

that the conduction band with lower energy (E_{g1}) corresponds to Mn $3d$ t_{2g} , and the conduction band with higher energy (E_{g2}) corresponds to Mn $3d$ e_g (Figure 9). Therefore, for both phases, Mn $3d$ orbitals overlap with O $2p$ orbitals in the valence band at the lower energy level of t_{2g} and e_g . In other words, the Mn $3d$ levels split into bonding and antibonding levels forming hybridized orbitals with ligand O $2p$ orbitals. Both phases of Mn_3O_4 are charge-transfer type insulators with characteristic band-splitting of the conduction band (Figure 3 and Figure 7).

IV. CONCLUSION

Electronic structures of Mn_3O_4 spinel and postspinel were systematically studied. *Ab initio* calculations and the optical measurements were performed on both phases, resulting in a consistent band structure with characteristic band-splitting of the conduction band. We obtained the band gap of 1.91(6) eV for the spinel phase, and 0.94(2) eV for the postspinel phase. Both phases of Mn_3O_4 are charge-transfer type insulators, and Mn $3d$ t_{2g} and O $2p$ form antibonding orbitals situated at the conduction band with higher energy. *Ab initio* calculations also demonstrate that Mn_3O_4 postspinel is a spin frustrated magnet.

V. ACKNOWLEDGEMENTS

This research is funded by the U.S. Department of Energy (DOE), Office of Basic Energy Sciences (BES). S.H. and W.L.M. are supported by the U.S. Department of Energy (DOE), Office of Basic Energy Sciences (BES), Division of Materials Sciences and Engineering, under Contact No. DE-AC02-76SF00515.

- ¹ B. Ammundsen, J. Desilvestro, T. Groutso, D. Hassell, J. Metson, E. Regan, R. Steiner, and P. Pickering, *J. Electrochem. Soc.* **147**, 4078 (2000).
- ² K. Ramesh, L. Chen, F. Chen, Z. Zhong, J. Chin, H. Mook, and Y. Han, *Catal. Commun.* **8**, 1421 (2007).
- ³ T. Maruyama and Y. Osaki, *J. Electrochem. Soc.* **142**, 3137 (1995).
- ⁴ G. Aminoff, *Z. Kristallogr.* **64**, 475 (1926).
- ⁵ Y. Xiao, D. E. Wittmer, F. Izumi, S. Mini, T. Graber, and P. J. Viccaro, *Appl. Phys. Lett.* **85**, 736 (2004).
- ⁶ M. Kim, X. M. Chen, X. Wang, C. S. Nelson, R. Budakian, P. Abbamonte, and S. L. Cooper, *Phys. Rev. B* **84**, 174424 (2011).
- ⁷ B. Boucher, R. Buhl, and M. Perrin, *J. Phys. Chem. Solids* **32**, 2429 (1971).
- ⁸ G. B. Jensen and O. V. Nielsen, *J. Phys. C* **7**, 409 (1974).
- ⁹ B. Chardon and F. Vigneron, *J. Mag. Mag. Mat.* **58**, 128 (1986).
- ¹⁰ E. Paris, C. R. II Ross, and H. Olijnyk, *Eur. J. Mineral.* **4**, 87 (1992).
- ¹¹ M. Merlini, M. Hanfland, M. Gemmi, S. Huotari, L. Simonelli, P. Strobel, *Am. Mineral.* **95**, 200 (2010).
- ¹² S. Hirai, A.M. dos Santos, M.C. Shapiro, J.J. Molaison, N. Pradhan, M. Guthrie, C.A. Tulk, I.R. Fisher, and W.L. Mao, *Phys. Rev. B* **87**, 014417 (2013).
- ¹³ R. Tackett, G. Lawes, B.C. Melot, M. Grossman, E.S. Toberer and R. Seshadri, *Phys. Rev. B* **76**, 024409 (2007).
- ¹⁴ T. Suzuki and T. Katsufuji, *Phys. Rev. B* **77**, 220402 (2008).
- ¹⁵ Y. Nii, H. Sagayama, H. Umetsu, N. Abe, K. Taniguchi, and T. Arima, *Phys. Rev. B* **87**, 195115 (2013).
- ¹⁶ M. Kim, X. M. Chen, Y. I. Joe, E. Fradkin, P. Abbamonte, and S. L. Cooper, *Phys. Rev. Lett.* **104**, 136402 (2010).
- ¹⁷ Y. Yafet and C. Kittel, *Phys. Rev.* **87**, 290 (1952).
- ¹⁸ A. Kuriki, Y. Moritomo, S. Xu, K. Ohoyama, K. Kato, and A. Nakamura, *J. Phys. Soc. Jpn.* **72**, 458 (2003).

- ¹⁹ J. H. Chung, K. H. Lee, Y. S. Song, T. Suzuki, and T. Katsufuji, *J. Phys. Soc. Jpn.* **82**, 034707 (2013).
- ²⁰ C. Nisoli, R. Moessner, and P. Schiffer, *Rev. Mod. Phys.* **85**, 1473 (2013).
- ²¹ M. V. Rozhdestvenskaya, V. A. Mokievskii, and V. A. Stogova, *Kristallografiya* **11**, 903 (1966).
- ²² A. Chartier, P. D'Arco, R. Dovesi, and V.R. Saunders, *Phys. Rev. B* **60**, 14042 (1999).
- ²³ C. Franchini, R. Podloucky, J. Paier, M. Marsman, and G. Kresse, *Phys. Rev. B* **75**, 195128 (2007).
- ²⁴ D.P. Dubal, D.S. Dhawale, R.R. Salunkhe, V.J. Fulari, and C.D. Lokhande, *J. Alloys Compd.* **497**, 166 (2010).
- ²⁵ A. Jha, R. Thapa, and K.K. Chattopadhyay, *Mater. Res. Bull.* **47**, 813 (2012).
- ²⁶ P. Kubelka and F. Munk, *Z. Tech. Phys. (Leipzig)* **12**, 593 (1931).
- ²⁷ P. E. Blochl, *Phys. Rev. B* **50**, 17953 (1994).
- ²⁸ G. Kresse and D. Joubert, *Phys. Rev. B* **59**, 1758 (1999).
- ²⁹ G. Kresse and J. Furthmüller, *Comput. Mater. Sci.* **6**, 15 (1996).
- ³⁰ G. Kresse and J. Furthmüller, *Phys. Rev. B* **54**, 11169 (1996).
- ³¹ J. P. Perdew, K. Burke, and M. Ernzerhof, *Phys. Rev. Lett.* **77**, 3865 (1996).
- ³² S. L. Dudarev, G. A. Botton, S. Y. Savrasov, C. J. Humphreys, and A. P. Sutton, *Phys. Rev. B* **57**, 1505 (1998).
- ³³ J. Heyd, G. E. Scuseria, and M. Ernzerhof, *J. Chem. Phys.* **118**, 8207 (2003).
- ³⁴ H. J. Monkhorst and J. D. Pack, *Phys. Rev. B* **13**, 5188 (1976).
- ³⁵ M. C. Toroker, D. K. Kanan, N. Alidoust, L. Y. Isseroff, P. Liao, and E. A. Carter, *Phys. Chem. Chem. Phys.* **13**, 16644 (2011).